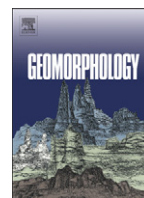




Contents lists available at ScienceDirect

## Geomorphology

journal homepage: [www.elsevier.com/locate/geomorph](http://www.elsevier.com/locate/geomorph)

# Tectonic geomorphology of the San Andreas Fault zone from high resolution topography: An example from the Cholame segment

J Ramón Arrowsmith<sup>\*</sup>, Olaf Zielke

School of Earth and Space Exploration, Arizona State University, Tempe, AZ 85287, USA

## ARTICLE INFO

### Article history:

Accepted 8 January 2009  
Available online xxxx

### Keywords:

Tectonic geomorphology  
LiDAR  
San Andreas Fault  
Digital Elevation Models

## ABSTRACT

High resolution topographic data along fault zones are important aids in the delineation of recently active breaks. A 15 km-long portion of the south-central San Andreas Fault (SAF) along the southern Cholame segment contains well preserved tectonic landforms such as benches, troughs, scarps, and aligned ridges that indicate recurring earthquake slip. Recently acquired LiDAR topographic data along the entire southern SAF (“B4” project) have shot densities of 3–4 m<sup>-2</sup>. Computed from the LiDAR returns, Digital Elevation Models (DEMs) of 0.25 to 0.5 m resolution using local binning with inverse distance weighting and 0.8 m or larger search radii depict the tectonic landforms at paleoseismic sites well enough to assess them confidently. Mapping of recently active breaks using a LiDAR-only based approach compares well with aerial photographic and field based methods. The fault zone varies in width from meters to nearly 1 km and is comprised of numerous en echelon meter to kilometer-length overlapping sub parallel fault surfaces bounding differentially moving blocks that elongate parallel to the SAF. The semantic variations of what constitutes “active” and the importance of secondary traces influence the breadth and complexity of the resulting fault trace maps.

© 2009 Elsevier B.V. All rights reserved.

## 1. Introduction

The south central San Andreas Fault (SAF; Fig. 1) is manifest at the surface by some of the most well preserved tectonic geomorphology at 10s to 1000s of meter scale in the world (Fig. 2; e.g., Wallace, 1975; Wallace and Schulz, 1983; Wallace, 1991). The troughs, ridges, sags, and offset channels along the zone have developed by the interaction of repeated slip along subparallel discontinuous roughly co-planar fault surfaces bounding the elongate blocks of the fault zone and the fluvial and hillslope processes operating on the surface (over at least the Holocene; Bryant and Hart, 2007). The features indicate a valuable record of the structural geology of the upper few kilometers of the fault zone (e.g., Lawson, 1908; Wallace, 1991; Arrowsmith, 2007) and of the history of earthquakes that have occurred along it over the last centuries to millennia (e.g., Grant and Sieh, 1994). These features are indicative of where the next earthquake is most likely to slip.

Characterizing the tectonic geomorphology of the SAF fault zone is valuable for numerous reasons. The geometry and motions of the blocks that comprise the upper few km of the fault zone inform studies of rupture dynamics, fluid flow along fault zones, fault zone strength, and evolution of fault zone fabrics (e.g., Scholz, 1991). Using landforms as markers of the horizontal and vertical motions along and across the fault zone, coupled with Quaternary geochronology, provides a measure of the strain release rate at centennial to

millennial time scales—a valuable bridge between geologic strain release rates at million year time scales and the geodetically measured strain accumulation rates at decadal time scales (e.g., Sieh and Jahns, 1984; Noriega et al., 2006). The meter scale geomorphology of the fault zone guides siting and interpretation of paleoseismic sites (e.g., McCalpin, 1996). Locating the excavations must be done by interpolation between landforms indicative of the active fault location. The stratigraphy exposed in the trenches is directly related to the site geomorphology. The map geometry of the fault traces indicates the distribution of fracturing to be expected in the trench exposures and whether or not the excavations span the entire fault zone. Information on the timing and slip per event in earthquakes that comes from paleoseismic investigations is an essential ingredient in earthquake rupture forecasts (e.g., 2007 Working Group on California Earthquake Probabilities, 2008). Finally, delineating sufficiently active and well defined fault zones is of practical value for anticipating ground rupture hazard for structures (e.g., Bryant and Hart, 2007).

Airborne Laser Swath Mapping (ALSM) and LiDAR-derived measurements of topography have recently been deployed for the extensive mapping of fault zone topography at unprecedented detail and coverage (e.g., Haugerud et al., 2003; Sherrod et al., 2004; Bevis et al., 2005; Kondo et al., 2008). These data are at the appropriate scale (meters) and accuracy (decimeters) to provide useful measurements of the fine features that record repeated earthquakes in the landscape. Typically, fault zones in the USA are mapped using USGS Quadrangle topographic maps and 10 or 30 m DEMs (<http://seamless.usgs.gov>; Fig. 2) and aerial photography (McCalpin, 1996; Bryant and Hart,

<sup>\*</sup> Corresponding author.

E-mail address: [Ramon.arrowsmith@asu.edu](mailto:Ramon.arrowsmith@asu.edu) (J.R. Arrowsmith).

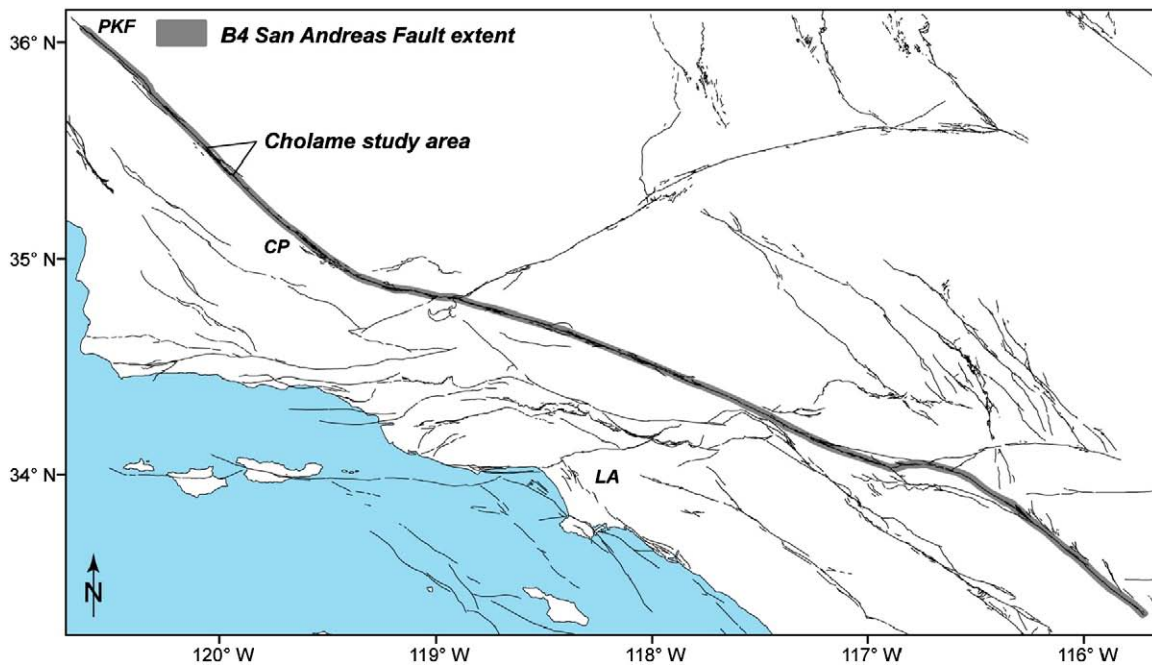


**Fig. 1.** Active faults of southern California (U.S. Geological Survey and California Geological Survey, 2006), the extent of the B4 San Andreas Fault (SAF) LiDAR data, and the Cholame study area along the SAF (extent of Fig. 2). LA is the location of Los Angeles, PKF is Parkfield, and CP is the Carrizo Plain.

2007). While aerial photographs certainly have meter scale resolution, and photogrammetry can be used to produce high resolution DEMs, they are typically only used in a 2-dimensional sense as base maps for locating fault traces and qualitatively in 3-dimensions for stereoscopically aided interpretation.

The recent imaging of the south-central SAF by the B4 project (Bevis et al., 2005; <http://www.earthsciences.osu.edu/b4>) provides many new opportunities to clarify our understanding of its structural geology, geomorphology, and recent deformation history. Examining how the new data can be optimally used for mapping recently active fault breaks, characterizing the setting of paleoseismic sites, and assessing the differences between fault trace mapping using traditional (pre-LiDAR) approaches and that done using the LiDAR topography are the major goals of this paper.

In this paper, we take our knowledge of a portion of the south-central SAF (southern Cholame segment; Figs. 1 and 2) based on prior fault trace mapping and paleoseismic work and combine it with analysis of the new LiDAR topographic data to explore its use in characterization of the SAF tectonic geomorphology. First, we examine which processing parameters produce optimal DEMs for characterizing the tectonic geomorphology. Secondly, we characterize the LY4 paleoseismic site (Stone et al., 2002; Young et al., 2002). Third, we compare “classic” field and airphoto-based mapping of recently active fault breaks along the study reach by Vedder and Wallace (1970) with representative field-based mapping done to prospect for the LY4 site (Stone et al., 1998; Stone, 1999), and new LiDAR-only mapping by co-author Zielke. The Cholame section we study presents a range of features and challenges. Results from this study have potential wide application to characterization of other faults scanned with LiDAR.

## 2. Previous tectonic geomorphology and paleoseismology studies

The south-central San Andreas Fault (SAF) comprises the predominantly seismogenic segments from Parkfield through the Cholame and Carrizo Plain (Fig. 1). It is notable for being the portion of the SAF with the largest total Miocene and later offset (~315 km; e.g. Sims, 1993), for the highest SAF slip rate (~35 mm year<sup>-1</sup> measured over the late Holocene; e.g., Sieh and Jahns, 1984), and for having apparently steady deep slip (below about 12 km) also at about

35 mm year<sup>-1</sup> (Noriega et al., 2006). It is also an iconic portion of the SAF with the well preserved tectonic geomorphology that indicates its activity. The troughs, scarps, benches, sags, and ridges that define the fault zone are readily visible from the air and now in high resolution LiDAR-derived topography.

Scientific efforts following the 1966 Parkfield earthquake included detailed mapping of the recently active fault breaks along the south-central SAF (Ross, 1969; Brown, 1970; Vedder and Wallace, 1970). The Vedder and Wallace mapping covers the Cholame and Carrizo Plain sections of the SAF. They noted that the SAF zone showed clear evidence for repeated recent fault slip (the most recent being the great 1857 earthquake). In addition, they concluded that the fault zone was comprised of more subparallel, continuous, and longer fault traces than the sections to the northwest (Brown, 1970) and southeast (Ross, 1969) and suggested that this was largely a result of the better preservation of the features because of the drier climate, but also because of possible variation in fault behavior.

Seismogenic strain release varies along the SAF with a transition from fully creeping north of Parkfield, to decreasing creep and M6 events at Parkfield (Toké and Arrowsmith, 2006), to completely locked with M>7 earthquakes recurring on 100–200 year time scales in the Cholame and Carrizo Plain (Grant and Sieh, 1994; Akciz et al., 2009). Slip in the 1857 earthquake was 1–2 m southeast of Parkfield, 3–5 m along the Cholame segment (Sieh, 1978; Lienkaemper, 2001; Young et al., 2002; however, it may have been higher locally, e.g., Runnerstrom et al., 2002), and up to 8 m in the Carrizo Plain (Sieh, 1978; Liu-Zeng et al., 2006; Arrowsmith and Zielke, 2008).

Given the historic precedent of the 1857 earthquake and its foreshocks, a deficit of slip of more than 4 m accumulated since 1857, and a major gap in paleoseismic sites northwest of their concentration in the Carrizo Plain, Arrowsmith and M.S. student Elizabeth Zima (né Stone; Stone, 1999) and Ph.D. student Jeri Young (Young, 2004) focused on the southern 15 km of the Cholame segment and developed a paleoseismic site called LY4 (Fig. 2). Arrowsmith, Stone, and colleagues originally mapped the recently active faults and tectonic geomorphology along that reach to identify LY4 (see below for more discussion of this mapping). The mapping results were reported in Stone (1999), while the paleoseismic results are in Stone et al. (2002) and Young et al. (2002). Evidence for at least three

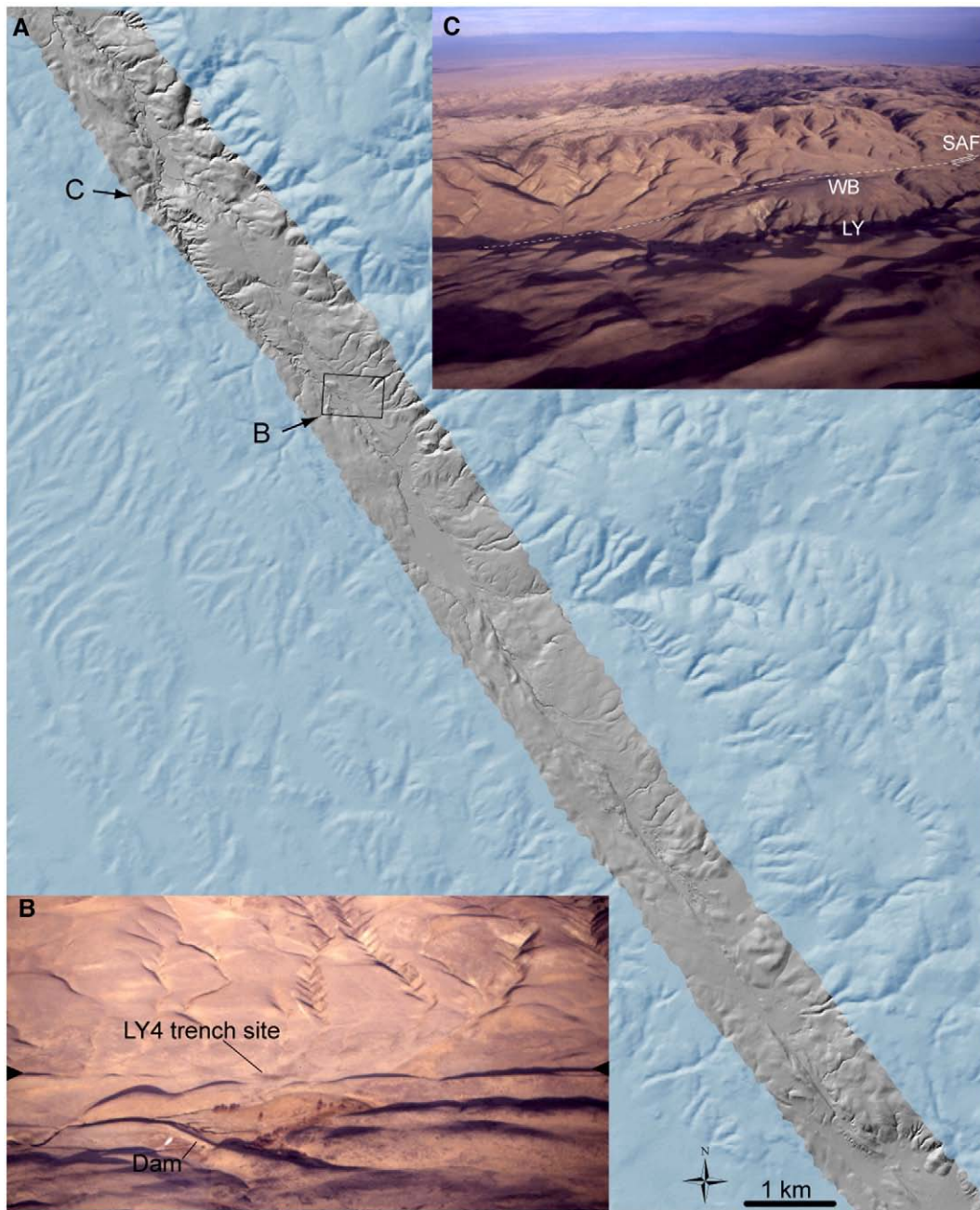


**Fig. 2.** A) 17 km long section of the SAF along the southern Cholame segment investigated in this study (see Fig. 1 for location; between 33 and 50 km southeast of California State Highway 46). Strip of the 0.5 m resolution hillshaded DEM from the B4 LiDAR dataset is shown in grey over the 10 m resolution NED (<http://seamless.usgs.gov>) hillshade in blue. The discontinuous traces of the SAF and the deflected offset and locally ponded drainages are clear in the LiDAR hillshade. Box shows location of the LY4 site (Figs. 3–6). View directions of B and C oblique aerial photographs are indicated. B) Oblique aerial photograph towards NE of the LY4 site showing the fault trace (between black triangles) and a dam that was built in the 1940s. C) Oblique aerial photograph towards ESE over the Whaleback pressure ridge (WB) and the Las Yeguas (LY) drainage where it has incised into the uplifting flank of the WB. A simplified SAF trace is dashed. (For interpretation of the references to colour in this figure legend, the reader is referred to the web version of this article.)

earthquakes since about 1030 A.D. including the 1857 event, and  $3 \pm 0.5$  m of slip in 1857 across a 5 m aperture was exposed in the numerous excavations at LY4.

### 3. The B4 southern San Andreas Fault laser scan data set

The southern San Andreas and the San Jacinto Fault zone were scanned with LiDAR in 2005 (Bevis et al., 2005; <http://www.earthsciences.osu.edu/b4>; Fig. 1). The goals of the project were to gather high precision topographic (and photographic) data to characterize near fault ground deformation in a future large earthquake, to support tectonic and paleoseismic studies, and to further

develop the integrated technologies and protocols (LiDAR, GPS, and IMU) necessary to routinely collect such research-grade data. An Optech ALTM 3100 was mounted in a Cessna 310 and flown at about 600 m above ground. The scanner was operated at 70 kHz with a  $20^\circ$  scan angle. The resulting swaths were about 430 m wide with 15 cm diameter laser spots. The stated shot spacing per swath was then 0.6 m at nadir and about 1 m at the edge of the swath. Typically, the plane made five passes to scan a total of 1–1.5 km wide zone spanning the SAF. The data were gathered by a team lead by Ohio State University that included USGS, the National Center for Airborne Laser Mapping (NCALM), and UNAVCO. The data have been made available publicly. In particular, the GEON project (<http://www.geongrid.org> or

<http://www.opentopography.org>), through the GEON LiDAR Workflow (Crosby et al., 2006; Jaeger-Frank et al., 2006), enables the scientific community access the raw point cloud and to produce Digital Elevation Models (DEMs) with user-defined resolution and other processing parameters (see below).

#### 4. Methods and analysis

##### 4.1. Digital Elevation Model preparation

Access to the point cloud from the B4 LiDAR scan permits us to explore the effect of the method of preparation and resolution of DEMs on their interpretability for tectonic geomorphology and earthquake geology studies. The DEM represents topography as measured by the heterogeneously distributed 3D laser returns as a two dimensional grid of elevation values spaced at a constant resolution. Computing the DEM from the scattered data is a computationally intensive, but relatively straightforward task. Many algorithms are available for these computations (e.g., El-Sheimy et al., 2005). Where the resolution is greater than the typical shot spacing, the DEM preparation method typically used is local binning (e.g., El-Sheimy et al., 2005; Kim et al., 2006) in which the value at a DEM node is a simple function (e.g., maximum, minimum, mean, and inverse distance weighted—IDW) of the points within a specified

search radius ( $r$ ). Increasing the search radius ensures that points will be found (otherwise a null is assigned at the grid node), but the value will represent a broader area (Fig. 3). Inverse distance weighting ( $1/r^2$ ) partially overcomes this problem by weighting nearer points more than farther ones (e.g., El-Sheimy et al., 2005). In cases where the resolution required is smaller than the shot density, interpolation is necessary. For this case, the local binning can work with large enough search radii, but typically methods such as spline, Kriging, and Triangular Irregular Networks (TINs) are used.

The average shot density at the LY4 study site is about  $3.6 \pm 1.1 \text{ m}^{-2}$ , ranging from 0 to more than  $10 \text{ m}^{-2}$  (Fig. 3E). This is a typical density for most of the B4 (Carrizo Plain and Salton Sea area as well; although we have not undertaken a systematic analysis). The density and qualitative evaluation of resulting DEMs suggests that 0.5 m DEMs are sufficiently well resolved for the local binning scheme. Four shots per square meter matches the number of nodes in a 0.5 m DEM. Using the local binning approach which we implemented including IDW (Kim et al., 2006) the question becomes, what is the optimal search radius for the favored IDW method? If there are no laser returns within the search radius, the DEM node at that location is returned as null (holes in the images in Fig. 3). As the search radius increases, the number of nulls goes down rapidly and asymptotically approach some minimum defined by anomalously large areas of no returns (water—bottom left of Fig. 3). Somewhere near that “shoulder” is an indicator of the proper

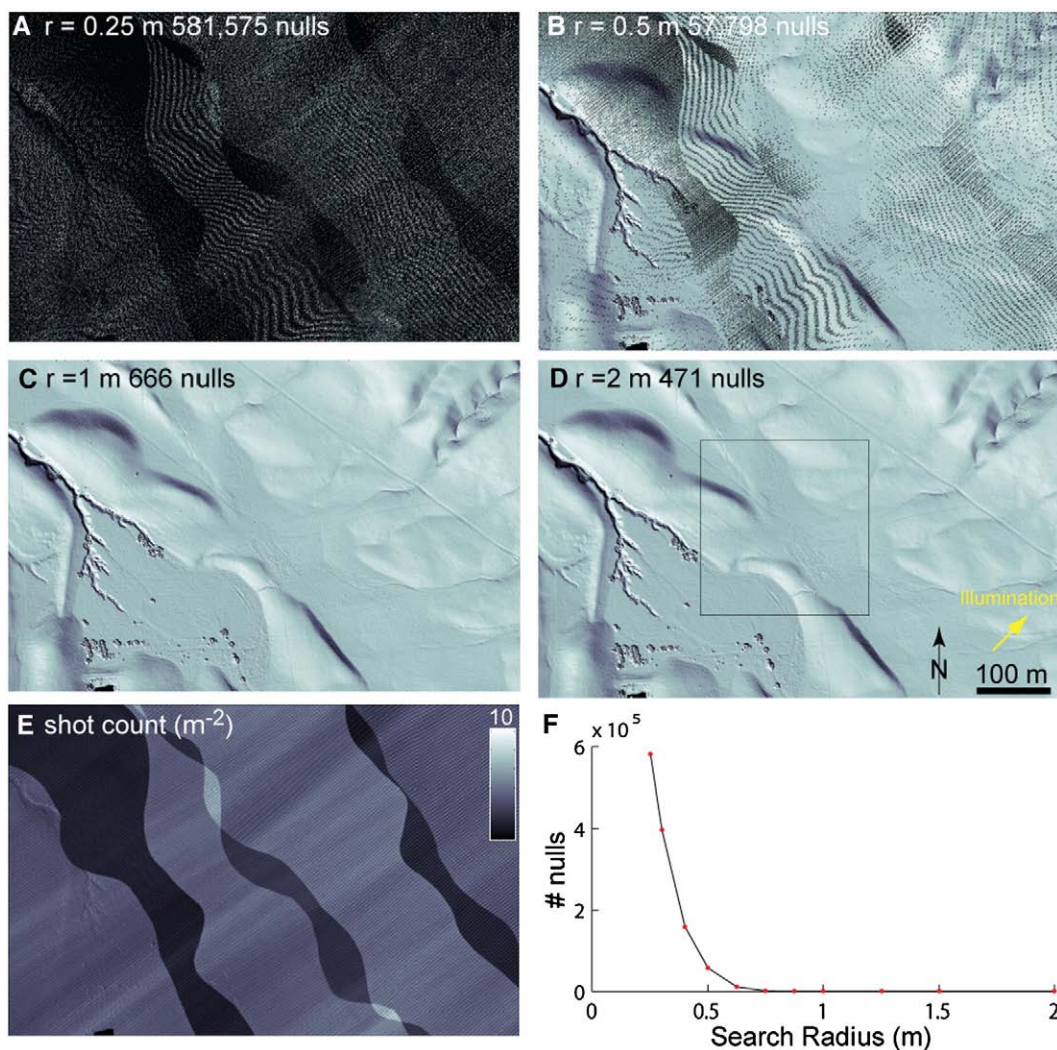


**Fig. 3.** Effect of search radius on local binning results in DEM production. DEMs of 0.5 m resolution are produced using inverse distance weighted local binning (Kim et al., 2006). As the search radius increases from 0.25 m (A) through 0.5 m (B), 1 m (C), and 2 m (D), the number of nulls (result from no laser returns in search radius) rapidly decreases (F). The heterogeneous shot count ( $\text{m}^{-2}$ ) of the area (E) results from multiple overlapping swaths from repeat overpasses. Box in D shows location of Fig. 4.

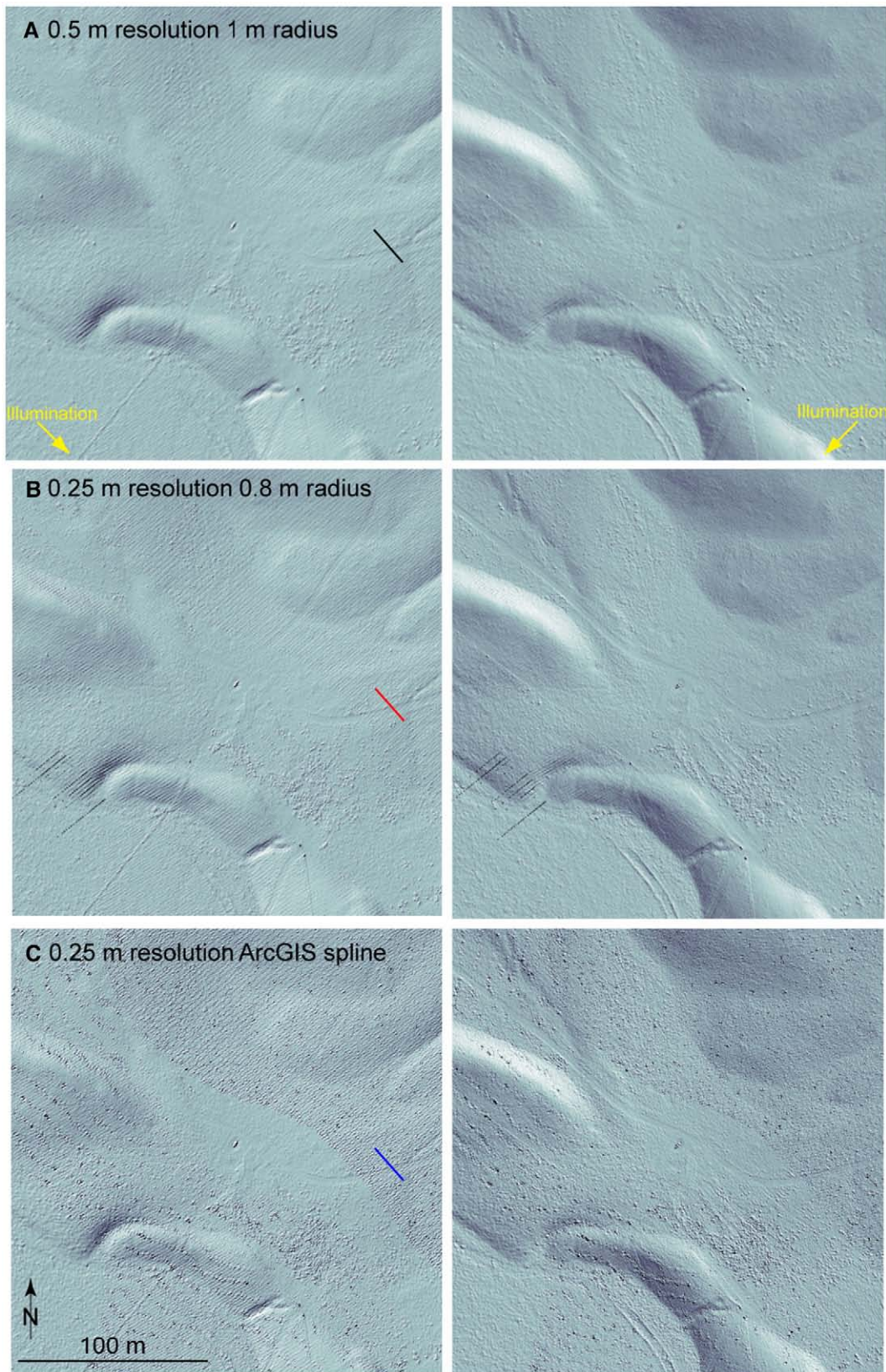


**Fig. 4.** Changing DEM resolution, illumination direction (N45W on left and N45E on right) and gridding algorithms at the LY4 site. A) 0.5 m IDW DEM with 1 m search radius has few nulls and is the product we typically analyze. B) 0.25 m IDW DEM with 0.8 m search radius has some nulls (NE-trending dark lineaments), and depicts the finer features slightly more clearly than A. See also Fig. 6. C) 0.25 m resolution DEM from ArcGIS spline has distracting artifacts, especially in areas of overlapping swaths. Black, red, and blue lines correspond to topographic profiles in Fig. 5. (For interpretation of the references to colour in this figure legend, the reader is referred to the web version of this article.)

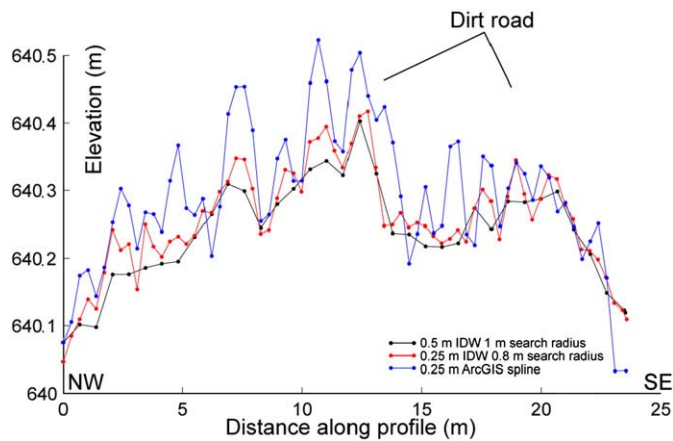


**Fig. 5.** Detailed topographic profiles from different DEMs (see location in Fig. 4). Each is from the same location but different data set. The convex upward alluvial fan form is evident, as is the flat dirt road, but the high frequency roughness shows the various manifestations of the “corduroy.” Corduroy is highest amplitude in the spline and most subdued for the coarser resolution 0.5 m DEM.

search radius. A search radius  $\sim 0.8$ – $1$  m simultaneously minimizes the number of null cells and the search radius (Fig. 3F).

While the argument just presented that 0.5 m DEMs are probably optimal in terms of resolution, what happens if we go to a finer resolution such as 0.25 m? File sizes go up by a factor of 4. Fig. 4 presents an exploration of the difference between the reference 0.5 m with 1 m search radius IDW and finer resolution 0.25 m DEMs computed with an IDW on a 0.8 m search radius and the default spline method from ArcGIS (<http://www.esri.com/software/arcgis>; regularized, weight of 0.1, and number of points is 12).

The spline-based DEM highlights the “corduroy” artifacts common in many LiDAR studies (Figs. 4 and 5). The repeated passes of the

aircraft have relative mislocations on the order of 0.1 m. These differences then are manifest in the point clouds and resulting DEMs as somewhat regular troughs and ridges normal to the flight direction with meter-scale wavelengths and decimeter amplitudes (Fig. 5). The spline method produces the deepest corduroy ( $\sim 20$  cm) while the IDW methods smooth it by a factor of two or more. With a 1 m search radius every 0.5 m, the coarser DEM has begun to average out the effects of the multiple swath mislocation. Illumination parallel to the scan direction ( $\sim N45E$ ; right panel of Figs. 4 and 6) diminishes the distraction of the corduroy for interpretation.

#### 4.2. Mapping of recently active breaks and tectonic geomorphology of the SAF

##### 4.2.1. Representative mapping approaches

We chose three representative approaches to fault trace mapping for assessment. Vedder and Wallace (1970) relied on systematic review of aerial photography and topographic maps with field checking for their 1:24,000 scale mapping of recently active breaks. This “classic” method is a reference against which we compare two other approaches. The first is field-based mapping on aerial photographic base maps done to prospect for the LY4 site (Stone et al., 1998; Stone, 1999). The second is new LiDAR-only mapping (no field checking) by co-author Zielke done for this study. These different approaches are commonly employed in active fault zone mapping. Our goal in this section is to qualitatively compare their depiction of the range of tectonic landforms along the Cholame section. Results from this study should be widely applicable to other faults for which LiDAR data are available.

##### 4.2.2. Vedder and Wallace (1970)

Vedder and Wallace (1970) present a sequence of 1:24,000 strip maps along the SAF between Cholame Valley and Tejon Pass, California. They used on-the-ground investigations and interpretation

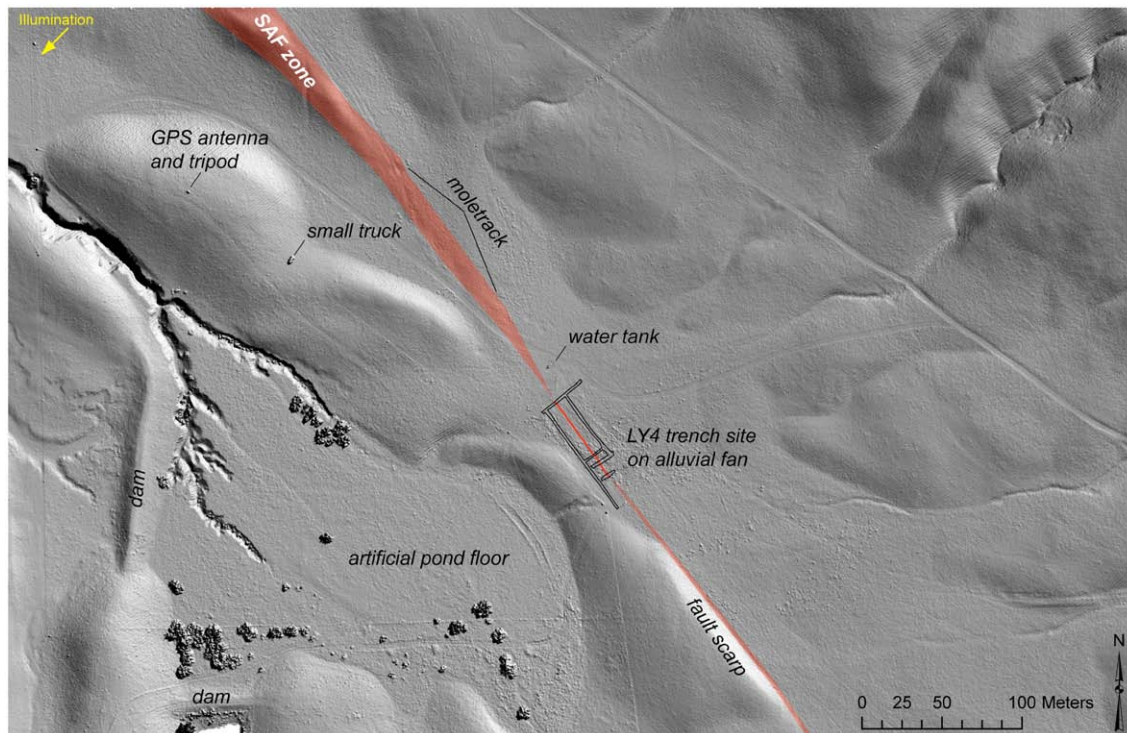


**Fig. 6.** Geomorphology of the LY4 paleoseismic site on 0.25 m IDW DEM computed with 0.8 m search radius. The recently active trace of the SAF is shown in red. It broadens in places where it is defined only by geomorphology such as the moletrack in the NW. In the trenches, we know exactly where it is. The trenches were sited here because young alluvial fan deposition regularly buries fault ruptures. Cultural features such as the water tank, dams, artificial pond floor, and small truck and GPS antenna and tripod (deployed for B4 data collection) give a sense of scale and resolution. (For interpretation of the references to colour in this figure legend, the reader is referred to the web version of this article.)

of vertical aerial photographs to delineate the traces of recently active fault breaks (Fig. 7). They recognized the recently active breaks in terms of the related geomorphic features: scarps, trenches or troughs, notches, parallel ridges, offset channels, sag ponds, ponded alluvium, undrained depressions, and shutter ridges. Their mapping included recently active breaks as solid lines (certain on Fig. 7) for which field or photographic evidence of recent motion was shown by scarps, trenches, sag ponds, spring lines, or vegetation contrasts. Less obvious features, but likely fault breaks, were dashed. They also provided brief notes identifying exemplary features. The data were compiled at 1:24,000 onto topographic quadrangle maps. They claim that features large enough to represent at this scale are generally accurate to within 50 ft (15.2 m) but may be as much as 150 ft (45.7 m) off in areas of lower relief. Zielke (this study) rectified scanned versions of the original Vedder and Wallace maps to provide an equivalent to US Geological Survey Digital raster Graphic (DRG) topographic maps and then digitized the mapping without reinterpretation or relocation.

#### 4.2.3. Stone and Arrowsmith

As part of our efforts to find a suitable paleoseismic site along the Cholame segment in the late 1990s, we (Stone, Arrowsmith, and other colleagues) mapped about 17 km of the fault zone (Stone et al., 1998; Stone, 1999; Fig. 7). This mapping included stereographic inspection of aerial photography from 1930 and field inspection and compilation on 1:10,000 printouts of the airphotos. We strictly limited the delineation of the active faults to those which showed evidence of recent motion by meter-scale topographic discontinuities. No features were mapped which were not identifiable in the field. Some alignments of features did not have clear indicators of sense of slip, but were most probably faults, so they were mapped as lineaments. This strictness results in fewer mapped features (Fig. 7) than Vedder and Wallace (1970) or Zielke (see below). We also mapped recently active landslides. The fault traces and landslide scarps and deposits were compiled and mapped onto aerial photographs rectified to the USGS DRGs (Stone, 1999). Arrowsmith (this study) re-rectified and re-digitized the relevant mapping for this study. Location accuracy for the Stone and Arrowsmith mapping is a few tens of meters.

#### 4.2.4. Zielke (this study)

Zielke used a fully digital, GIS-based approach without any field checking and relied only on DEMs (0.5 m with a 1 m search radius for the IDW) and derivative hillshades of the B4 LiDAR survey for his mapping, the relevant portion of which is presented in Fig. 7. He mapped landslide scarps and deposits as single polygons. He looked at fault scarps, offset and deflected features (mostly drainages), and other lineaments to define the fault trace. He distinguished between main and secondary fault traces (red and blue respectively in Fig. 7). A quality rating distinguishes between 'certain,' 'uncertain,' 'inferred,' and 'queried' features. The main trace was identified as the single trace most likely active during the last earthquake in 1857. It has a well developed surface expression with clear fault scarps and drainage deflection and offsets. If multiple, parallel fault strands were present, the active trace was identified as the one that has the least degraded features. The secondary traces are clearly recognizable, but probably inactive recently or have low rates of slip. These features are typically subparallel to the main trace and are at times several hundred meters away from it, indicating the integrated width of the fault zone as a whole is larger than that is active in just the last few earthquakes. Certain features (either main or secondary) are clearly identifiable lineaments along well expressed fault scarps or offset landforms. Uncertain features are less well expressed and typically do not show evidence of offset. Uncertain is the best rating that a secondary trace will usually receive. Inferred features are those without clearly indicated recent motion, but along the extension of certain or uncertain features or buried by young alluvium. Finally, queried

features are expressed only by weak lineaments sometimes beyond the ends of more certain features.

## 5. Results

### 5.1. Paleoseismic site analysis—LY4 site

Any effort to select a site for detailed paleoseismic analysis (e.g., trenching across a fault) requires an understanding of the context that comes from assessment of the topography around it. In this example, we use the B4 data to characterize the LY4 site after the fact (Stone et al., 2002; Young et al., 2002; Figs. 3–6). The two IDW DEMs (Fig. 4A, B) with illumination from the NE show the tectonic geomorphology of the site well. The 0.25 m resolution IDW DEM with the 0.8 m search radius (Fig. 4B) shows the site most clearly, even though some of the vegetation, fine topographic roughness and corduroy can be distracting. Fig. 6 takes that the 0.25 m resolution DEM with the N45E illumination, puts the similarly illuminated 0.5 m hillshade underneath to fill the nulls evident in Fig. 4B, and presents the tectonic geomorphology of the site. The trace of the SAF is clearly indicated by the en echelon troughs of the moletrack in the NW and the fault scarp to the SE (Fig. 6). The alluvial fan in the center has buried the repeated ground ruptures at the site making it a good location for paleoseismology (Stone et al., 2002; Young et al., 2002). Fine features such as the water tank and the vegetation on the alluvial fan near the trench site become clearer with the finer resolution (compare Fig. 4A and B).

### 5.2. Fault zone mapping

In the following subsections, we compare and contrast the Vedder and Wallace, Stone and Arrowsmith, and Zielke fault trace mapping in their depictions of the tectonic geomorphology of the SAF (Fig. 7).

#### 5.2.1. Northwest—Fig. 7B

The northwestern 6 km of the fault zone (Fig. 7B) preserves important fault zone discontinuities, distributed deformation, and the LY4 site. Vedder and Wallace show a fault zone varying in width from a single strand to 735 m. Stone and Arrowsmith note the greater width of the stepover (~100 m) as well as nearly 200 m width near LY4 indicated by two subparallel traces (see below). Zielke's active traces are singular except for the stepover. Considering the secondary traces, the fault zone is 300–500 m wide.

The Whaleback (WB on Fig. 7B; see also Fig. 2B) is an informally named recently uplifted block bounded largely on the NE by active traces of the SAF. The drainage that crosses it (just SE of the WB label) has recently been defeated with runoff joining the main NW-flowing Las Yeguas drainage to the SE. Other subtle traces of former drainages crossing Whaleback are evident in the field and in some illuminations of the LiDAR DEMs. The uplift of the Whaleback apparently pushes the Las Yeguas creek to the SW, and promotes incision along it. The formation of numerous landslides (mapped by Stone/Arrowsmith and Zielke) attest to the recent uplift and incision. The NW end of the Whaleback is marked by a prominent left step in the active fault traces (Stone/Arrowsmith and Zielke). Stone (1999) interpreted the uplift of the Whaleback as resulting from a possibly greater fault-normal width at depth of this stepover. Vedder and Wallace and to a lesser extent Zielke delineate the fault zone to the NW of the Whaleback with discontinuous swales and scarps.

The LY4 site is located in a portion of the fault zone marked by straight and continuous overlapping traces and where the Las Yeguas Creek enters the Whaleback-driven knickpoint (see above and Fig. 6 for more details). An important concern for the LY4 paleoseismic results is the degree of recent activity along the second fault trace at the site (to the SW). Both Stone et al. (2002) and Young et al. (2002) dismissed it as not significant in terms of accommodation of slip. All three of the mapping datasets show it, but with variable activity

ratings. Young et al. (2002) determined that the main trace accommodated about 3 m of slip in 1857. Lienkaemper (2001) and Arrowsmith and Zielke (2008) conclude that this is on the lower end of the likely slip released in 1857 over this reach as indicated by offset channels and other landforms. Could the secondary trace actually have accommodated the additional 1–2 m of slip? Young et al. (2002) concluded that it has not been recently active as indicated by

degraded fault scarps and undeformed inferred Holocene deposits (present west-northwest of the trench site). Review of the LiDAR-based imagery and mapping (Fig. 7B) suggests that this weakly defined trace has not undergone more than a few meters of slip during the 10s of kyr development of the landforms there (e.g., Arrowsmith et al., 1998), suggesting that it did not accommodate meter-scale slip in 1857.

### A Explanation for fault strip mapping

#### Vedder and Wallace, 1970

- Local features with annotation
- Regional features
- Recently active breaks, certain
- - - Recently active breaks, less obvious
- Ponds and lakes

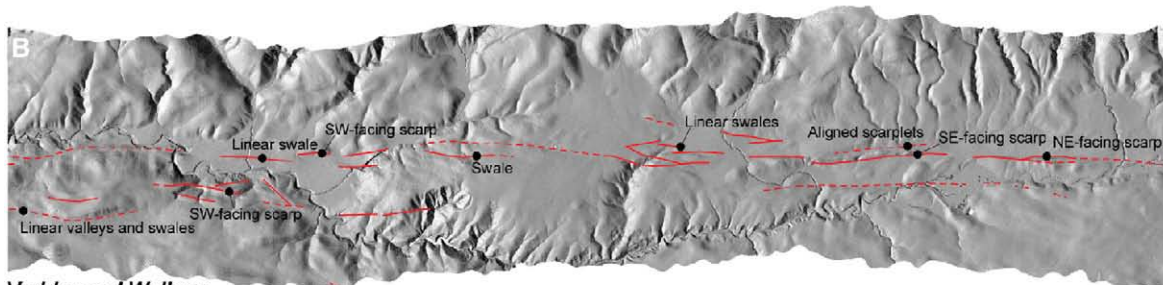
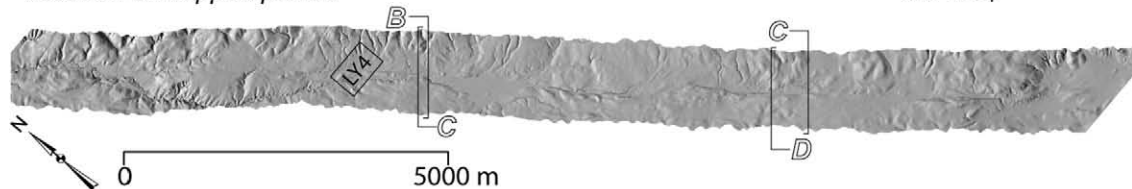
#### Stone and Arrowsmith

- Fault trace
- - - Fault trace, concealed
- - - Fault trace, inferred
- Lineament
- Landslide deposit
- Landslide scarp
- Sag

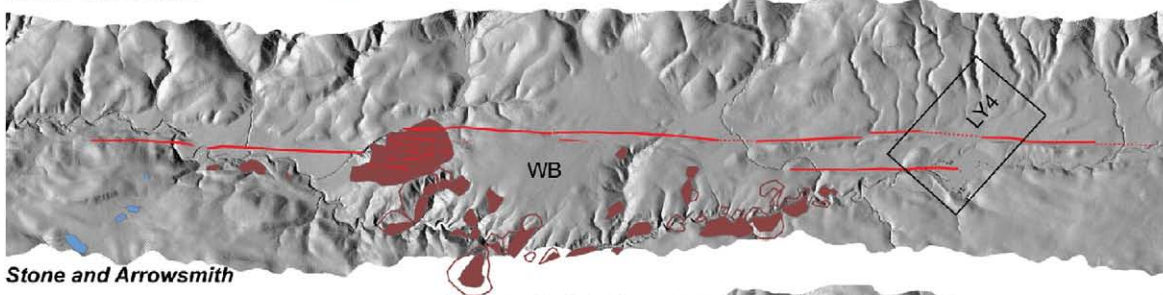
#### Zielke, this study

- Fault traces: red for main trace, blue for secondary traces
- Fault trace, certain
- - - Fault trace, inferred
- - ? - Fault trace, queried
- - - - Fault trace, uncertain
- Landslide deposit and scarp

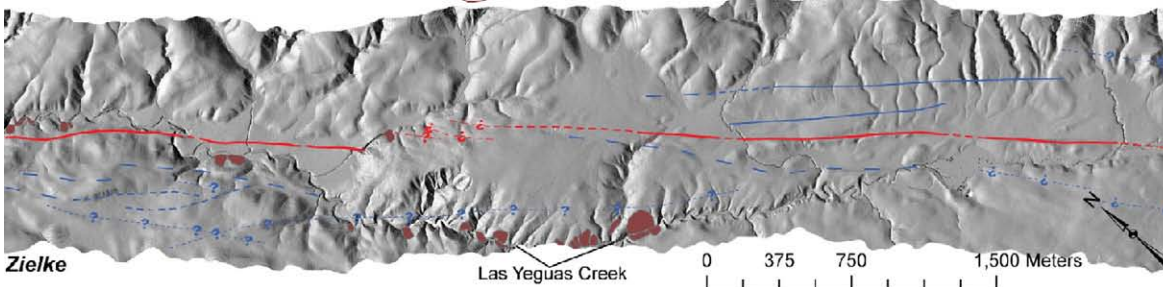
#### Location of mapped panels



Vedder and Wallace



Stone and Arrowsmith



Zielke

Fig. 7. Fault strip mapping by Vedder and Wallace (1970); Stone and Arrowsmith (Stone, 1999); and Zielke, this study. A) Explanation for symbology and locations of the mapped panels that follow. B) Northwestern, C) central, and D) southeastern mapped panels showing the three different mapping results overlain on 0.5 m DEMs with N45W illumination. The location of the LY4 paleoseismic site (e.g., Stone et al., 2002; Young et al., 2002; Figs. 4–6) is also indicated in A and B. See text for explanation.

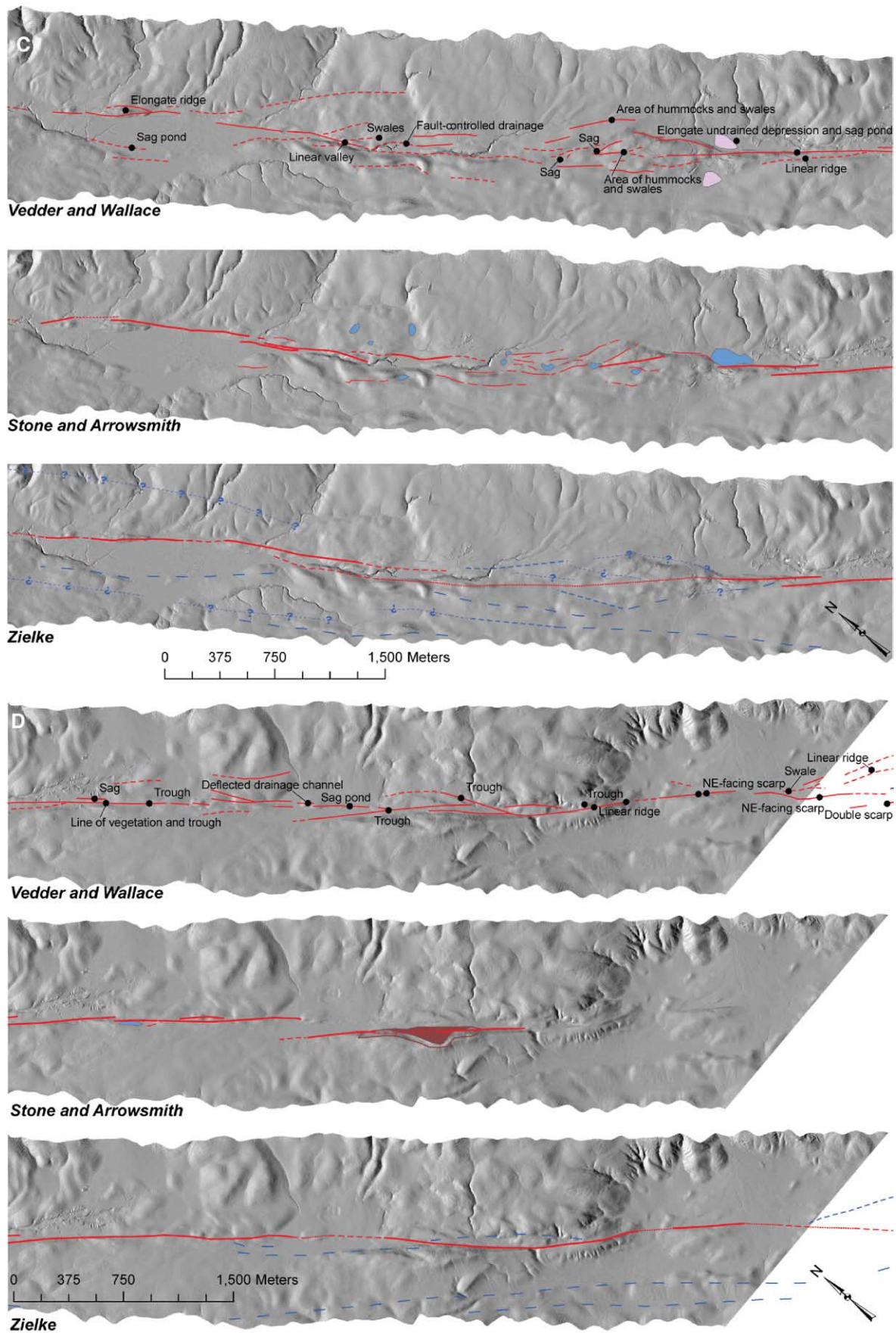
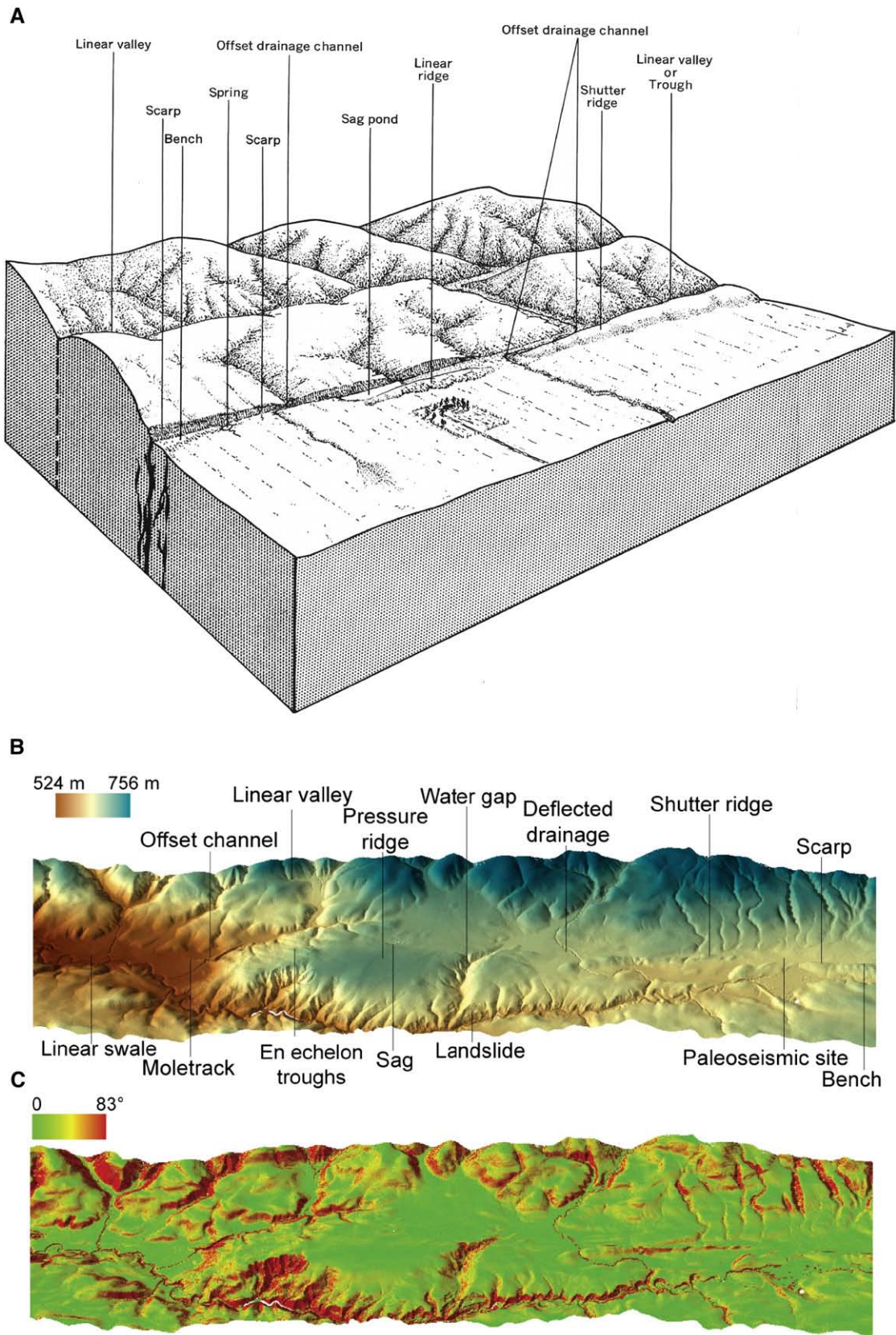


Fig. 7 (continued).



**Fig. 8.** Common landforms produced along recently active strike-slip faults such as the south-central San Andreas Fault. A) Classic block diagram from [Vedder and Wallace \(1970\)](#). B) LiDAR DEM-based oblique view (4.5 km long) of an exemplary piece of topography color-coded by elevation showing all features of A along with a few more mostly associated with the distributed deformation of the Whaleback pressure ridge (water gap and landslide in this case). C) Slope map showing the quantitative interpretative power that can come from these topographic data. B and C come from the area of [Fig. 7B](#), but are meant to be broadly representative.

### 5.2.2. Central—Fig. 7C

The central 6 km of mapping is notable for a potential paleoseismic site in the northwest, important fault controlled drainage, short discontinuous and variably oriented faults in the middle, and a transition to straight and longer fault traces to the southeast. Vedder and Wallace's fault widths here are about 300 m. Stone and Arrowsmith show simple traces in the northwest and southeast bounding a ~150 m wide lineament-dominated belt. Zielke's active traces are uncertain through the central discontinuities, whereas the secondary traces show an overall fault zone with decreasing from 750 m in the NW of this section to just a single few meters wide trace in the SE.

Vedder and Wallace note the large sag pond in the NW of the map. Stone (1999) calls this the "Las Yeguas site." It is a good potential paleoseismic site (Stone et al., 1998). As all the maps show, the fault traces cross alluvial fans feeding the marshy sag from the NE.

The fault-controlled drainage identified by Vedder and Wallace confounded the field mapping by Stone and Arrowsmith. We had a hard time differentiating fluvial and fault scarps there. Just to the SE of the fault controlled drainage, the fault zone becomes even more complex. Vedder and Wallace denoted "area of hummocks and swales." Stone and Arrowsmith noted that no faults were conspicuous. Zielke can only draw an uncertain main fault through the center, while his secondary faults pick up the greater width of the fault zone. The LiDAR topography is consistent with what Stone/Arrowsmith and Vedder/Wallace maps show as sags between ridges. This zone appears to comprise ~10 discontinuous fault blocks. The blocks have moved differentially—some up and some down—to produce the notable sags and ridges. Stone (1999) interpreted this zone in 3-dimensions as one in which the fault surfaces were "petals" of a flower structure which flared upward from a more continuous through going fault surface (its buried trace perhaps delineated by Zielke). If it exists, the depth of flaring is probably on the order of the horizontal extent of the features (several hundred meters).

### 5.2.3. Southeast—Fig. 7D

The south easternmost 5 km of the mapped fault zone is marked by greater geometric simplicity than the portions to the NW. Vedder and Wallace show a 50–100 m wide zone of sags, troughs, and ridges. Stone and Arrowsmith show 1–2 km long stepping fault traces with a landslide-dominated 30 m high fault scarp. Zielke's gently curving traces show a ~100 m left bend heading off the map to the SE (also shown in the Vedder and Wallace mapping). Zielke's secondary traces are ~1 km long and subparallel with the main trace and delineate a ~500 m wide fault zone.

## 6. Discussion

The suite of landforms that indicates the recent activity of a strike-slip fault is illustrated in "textbook" form in Fig. 8A. Any landform in isolation (i.e., bench, scarp, or trough) is not sufficient to delineate the active fault. The landforms taken together in terms of their spatial association and orientation are a strong predictor of fault location (as indicated by historic earthquake surface ruptures which have occurred along such belts of topographic features and the paleoseismic trenches which have been sited accordingly and successfully exposed evidence of recent faulting). Using GIS visualization tools like ArcScene (<http://www.esri.com/software/arcgis>) makes it possible to update such a figure and to show a few new features (Fig. 8B). Either Fig. 8A or B is a sufficient summary of the landforms produced along recently active faults, but Fig. 8B shows them with greater realism and detail. Whether or not that makes a difference for training researchers and students to identify such features remains to be seen. But, they can use such visualization tools to interact with these data from numerous virtual view points and with different color ramps, or other manipulations.

This paper represents an early analysis of the utility of high resolution topographic data now becoming readily available along such faults as the SAF. We have applied this analysis to paleoseismic site evaluation and fault trace mapping (given the caveat that the active fault zone may be broader than the data coverage). Quantitative and systematic analysis of offset stream channels and other features (i.e., Sieh, 1978; Lienkaemper, 2001) is underway (Arrowsmith et al., 2006; Arrowsmith and Zielke, 2008).

The different mapping results show that most of the primary features are robustly manifest. We do not advocate mapping without visiting the field. Such a recommendation is not new because Vedder/Wallace and Stone/Arrowsmith inspected aerial photographs in advance of the field work. Any such inspection is an efficient step. The LiDAR DEMs provide an additional, useful, and well georeferenced dataset. Indeed, the georeferencing of the LiDAR is significantly better (probably at least an order of magnitude more accurate) than the commonly available 1 m USGS digital orthophoto quarter quadrangles. Thus, digitizing before, during, and after field inspection using LiDAR DEMs and derivatives as base maps will improve the geolocation quality of the resulting maps.

The B4 LiDAR coverage is in a largely unforested portion of Southern California. The data are not classified in terms of ground and vegetation returns. The SAF and related faults in northern California and elsewhere are spectacularly exposed in "bare earth" DEMs (e.g., Haugerud et al., 2003; Sherrod et al., 2004; Kondo et al., 2008). In such conditions, the advantage of LiDAR is even greater than discussed here.

This study is largely qualitative and subjective (as is required for siting and mapping). The eyes and mind of a geologist/geomorphologist are the most valuable tools. LiDAR analyzed within a facile GIS environment is a powerful aid. Moving beyond these "pretty pictures" will produce new understanding about rates and processes through the interaction of the hillslope, landsliding and fluvial surface processes with the faulting and distributed deformation. The high slopes along Las Yeguas Creek as it passes through the Whaleback uplift zone are clear in Fig. 8C and consistent with the mapped concentration of landslides there (Stone/Arrowsmith and Zielke mapping, Fig. 7B). Narrow swaths of higher slopes show the recently active fault traces around LY4 and NW (left) of the Whaleback. Fault scarps indicate that trace and could be morphologically dated (Arrowsmith et al., 1998). Significantly extending such musings, Hilley and Arrowsmith (2008) used the LiDAR DEMs and knowledge of the tectonic activity of a pressure ridge along the SAF in the Carrizo Plain to depict landscape development in an area of transient rock uplift.

## 7. Conclusions

Swaths of high resolution topographic data along fault zones are important aids in the delineation of recently active breaks. LiDAR data such as the B4 southern SAF laser scan has shot densities of 3–4 m<sup>-2</sup> and can be gridded to 0.25 to 0.5 m resolution using local binning with inverse distance weighting and 0.8 m or larger search radii. Those resolutions depict the tectonic landforms at paleoseismic sites well enough to assess them confidently. Mapping of recently active breaks using a LiDAR-only based approach compares well with a combination of aerial photographic and field-based methods. But LiDAR, field, and spectral imaging (i.e., aerial photography) will give the best results. The semantic variations of what constitutes "active" and the importance of secondary traces influence the breadth and complexity of the resulting fault trace maps. The Cholame section we have studied presents a range of tectonic features and challenges. These analyses are applicable to similar kinds of studies along the SAF and other active faults for which LiDAR topography data are or may become available.

## Acknowledgements

We thank Elizabeth Zima (néé Stone) for her careful Cholame segment mapping and compilation. Jeri Young's (re)consideration of

features near LY4 was valuable. Vince Matthews, George Hilley, and others made important contributions to the mapping. The Twisselmanns, Silks, and Pritchards generously permitted us access to their land. We also thank Dallas Rhodes and Nathan Toké for the insightful geomorphologic and paleoseismological discussions. The B4 project is a bold concept that produced amazing data. Thanks to Mike Bevis, Ken Hudnut, and the numerous others at the Ohio State University, US Geological Survey, the National Center for Airborne Laser Mapping, and UNAVCO. This research was motivated by capabilities available through the GEON LiDAR Workflow. Thanks to Chris Crosby for sharing that vision and for numerous discussions about the tectonic geomorphology of the SAF as manifest in LiDAR topography. Reviews by Hisao Kondo, Richard Whittecar, and Takashi Oguchi were very helpful. This effort was supported partially by NSF grants (EAR-0225543, EAR-0310357, EAR-0409745, and EAR-0711282), Geo-Earthscope, and the Southern California Earthquake Center (SCEC).

## References

- 2007 Working Group on California Earthquake Probabilities, 2008. The Uniform California Earthquake Rupture Forecast, version 2 (UCERF 2). U.S. Geological Survey Open-File Report 2007-1437 and California Geological Survey Special Report 203. [<http://pubs.usgs.gov/of/2007/1437/>].
- Akciz, S.O., Grant Ludwig, L., Arrowsmith, J.R., 2009. Revised dates of large earthquakes along the Carrizo section of the San Andreas Fault, California, since A.D. 1310±30. *J. Geophys. Res.* 114, B01313. doi:10.1029/2007JB005285.
- Arrowsmith, J.R., 2007. Structural geology, tectonic geomorphology, and recent slip history of the south-central San Andreas Fault. Geological Society of America Annual Meeting, Paper No. 155-3.
- Arrowsmith, J.R., Zielke, O., 2008. Slip along the San Andreas Fault associated with the great 1857 earthquake derived from "B4" LiDAR high resolution topographic data. *Eos Transactions AGU* 89 (53) Fall Meet. Suppl., Abstract T44B-03.
- Arrowsmith, J.R., Rhodes, D.D., Pollard, D.D., 1998. Morphologic dating of scarps formed by repeated slip events along the San Andreas Fault, Carrizo Plain, California. *Journal of Geophysical Research* 103, 10,141–10,160.
- Arrowsmith, J.R., Campbell, B., Crosby, C., Raleigh, D., 2006. Tectonic geomorphology and earthquake geology of the 1857 reach of the San Andreas Fault: a new look from Airborne Laser Swath Mapping. *Eos Transactions AGU* 87 (52) Fall Meet. Suppl., Abstract G53C-0916.
- Bevis, M., Hudnut, K., Sanchez, R., Toth, C., Grejner-Brzezinska, D., Kendrick, E., Caccamise, D., Raleigh, D., Zhou, H., Shan, S., Shindle, W., Yong, A., Harvey, J., Borsa, A., Ayoub, F., Elliot, B., Shrestha, R., Carter, B., Sartori, M., Phillips, D., Coloma, F., Stark, K., 2005. The B4 Project: scanning the San Andreas and San Jacinto fault zones. *Eos Transactions AGU* 86 (52) Fall Meet. Suppl., Abstract H34B-01.
- Brown Jr., R.D., 1970. Map showing recently active breaks along the San Andreas and related faults between the northern Gabilan Range and Cholame valley, California. U.S. Geological Survey Miscellaneous Geologic Investigations Map I-575, scale 1:62,500.
- Bryant, W.B., Hart, E., 2007. Fault-rupture hazards zones in California: Alquist-Priolo Earthquake Fault Zoning Act with index to earthquake fault zones. Department of Conservation, California Geological Survey, Special Publication 42.
- Crosby, C.J., Arrowsmith, J.R., Frank, E., Nandigam, V., Kim, H.S., Conner, J., Memon, A., Baru, C., 2006. Enhanced access to high-resolution LiDAR topography through cyberinfrastructure-based data distribution and processing. *Eos Transactions AGU* 87 (52) Fall Meet. Suppl., Abstract IN41C-04.
- El-Sheimy, N., Valeo, C., Habib, A., 2005. Digital Terrain Modeling: Acquisition, Manipulation, and Applications. Artech House, Boston.
- Grant, L.B., Sieh, K., 1994. Paleoseismic evidence of clustered earthquakes on the San Andreas Fault in the Carrizo Plain, California. *Journal of Geophysical Research* 99 (B4), 6819–6841.
- Haugerud, R.A., Harding, D.J., Johnson, S.Y., Harless, J.L., Weaver, C.S., Sherrod, B.L., 2003. High-resolution Lidar topography of the Puget Lowland, Washington—a bonanza for earth science. *GSA Today*, Geological Society of America 13 (6), 4–10.
- Hilley, G.E., Arrowsmith, J.R., 2008. Geomorphic response to uplift along the Dragon's Back pressure ridge, Carrizo Plain, California. *Geology* 36. doi:10.1130/G24517A.1.
- Jaeger-Frank, E., Crosby, C.J., Memon, A., Nandigam, V., Arrowsmith, J.R., Conner, J., Altintas, I., Baru, B., 2006. A three tier architecture for LiDAR interpolation and analysis. *Lecture Notes in Computer Science* 3993, 920–927.
- Kim, H., Arrowsmith, J.R., Crosby, C.J., Jaeger-Frank, E., Nandigam, V., Memon, A., Conner, J., Baru, C., 2006. An efficient implementation of a local binning algorithm for digital elevation model generation of LiDAR/ALSM dataset. *Eos Transactions AGU* 87 (52) Fall Meet. Suppl., Abstract G53C-0921.
- Kondo, H., Toda, S., Okamura, K., Takada, K., Chiba, T., 2008. A fault scarp in an urban area identified by LiDAR survey: a Case study on the Itoigawa–Shizuoka Tectonic Line, central Japan. *Geomorphology* 101, 731–739.
- Lawson, A.C., 1908. Report of the Earthquake Investigation Commission upon the California Earthquake of April 18, 1906. Carnegie Institution, Washington D.C.
- Lienkaemper, J.J., 2001. 1857 slip on the San Andreas fault southeast of Cholame. *Bulletin of the Seismological Society of America* 91, 1659–1672.
- Liu-Zeng, J., Klinger, Y., Sieh, K., Rubin, C., Seitz, G., 2006. Serial ruptures of the San Andreas fault, Carrizo Plain, California, revealed by three-dimensional excavations. *J. Geophys. Res.* 111, B02306. doi:10.1029/2004JB003601.
- McCalpin, J., 1996. Paleoseismology. Academic Press, San Diego.
- Noriega, G.R., Arrowsmith, J., Grant, L.B., Young, J.J., 2006. Stream channel offset and late Holocene slip rate of the San Andreas Fault at the Van Matre Ranch site, Carrizo Plain, California. *Bulletin of the Seismological Society of America* 96, 33–47.
- Ross, D.C., 1969. Map showing recently active breaks along the San Andreas Fault between Tejon Pass and Cajon Pass, southern California. U.S. Geological Survey Miscellaneous Geologic Investigations Map I-553, scale 1:24,000.
- Runnerstrom, E.E., Grant, L.B., Arrowsmith, J.R., Rhodes, D.D., Stone, E.M., 2002. Displacement across the Cholame segment of the San Andreas Fault between 1855 and 1896 from cadastral surveys. *Bulletin of the Seismological Society of America* 92, 2659–2669.
- Scholz, C.H., 1991. The Mechanics of Earthquakes and Faulting. Cambridge University Press, Cambridge.
- Sherrod, B.L., Brocher, T.M., Weaver, C.S., Bucknam, R.C., Blakely, R.J., Kelsey, H.M., Nelson, A.R., Haugerud, R.A., 2004. Holocene fault scarps near Tacoma, Washington, USA. *Geology* 32, 9–12.
- Sieh, K.E., 1978. Slip along the San Andreas fault associated with the great 1857 earthquake. *Bulletin of the Seismological Society of America* 68, 1421–1448.
- Sieh, K.E., Jahns, R.H., 1984. Holocene activity of the San Andreas fault at Wallace Creek, California. *Geological Society of America Bulletin* 95, 883–896.
- Sims, J.D., 1993. Chronology of displacement on the San Andreas fault in central California: evidence from reversed positions of exotic rock bodies near Parkfield, California. In: Powell, R.E., Weldon II, R.J., Matti, J.C. (Eds.), *The San Andreas Fault System: Displacement, Palinspastic Reconstruction, and Geologic Evolution*. GSA Memoir, vol. 178. Geological Society of America, Boulder.
- Stone, E.M., 1999. Geomorphology, Structure and Paleoseismology of the Central Cholame Segment, Carrizo Plain, California. M.S. Thesis, Arizona State University, Tempe.
- Stone, E.M., Arrowsmith, J.R., Rhodes, D.D., Grant, L.B., 1998. Fault zone geometry and historic displacement along the Cholame segment of the San Andreas Fault, southern California. *Eos Transactions AGU* 79, 45 612.
- Stone, E., Grant, L.B., Arrowsmith, J.R., 2002. Recent rupture history of the San Andreas fault southeast of Cholame in the northern Carrizo Plain, California. *Bulletin of the Seismological Society of America* 92, 983–997.
- Toké, N.A., Arrowsmith, J.R., 2006. Reassessment of a slip budget along the Parkfield segment of the San Andreas Fault. *Bulletin of the Seismological Society of America*, Special Issue on the 2004 Parkfield Earthquake and Parkfield Experiment 96 (4B), S339–S348.
- U.S. Geological Survey and California Geological Survey, 2006. Quaternary Fault and Fold Database for the United States. accessed July 20, 2008, from USGS web site: <http://earthquake.usgs.gov/regional/qfaults/>.
- Vedder, J.G., Wallace, R.E., 1970. Map showing recently active breaks along the San Andreas and related faults between Cholame valley and Tejon Pass, California. U.S. Geological Survey Miscellaneous Geologic Investigations Map I-574, scale 1:24,000.
- Wallace, R.E., 1975. The San Andreas fault in the Carrizo Plain–Temblor Range region, California. In: Crowell, J.C. (Ed.), *San Andreas Fault in Southern California: A Guide to San Andreas Fault from Mexico to Carrizo Plain*. California Division of Mines and Geology Special Report, vol. 118, pp. 241–250.
- Wallace, R.E., 1991. The San Andreas Fault System, California. U.S. Geological Survey, Professional Paper 1515. United States Government Printing Office, Washington D.C.
- Wallace, R.E., Schulz, S.S., 1983. Aerial views in color of the San Andreas fault, California. U.S. Geological Survey Open File Report 83-98.
- Young, J.J., 2004. Characterization of Fault Behavior Along the Central San Andreas Fault, California. Ph.D. dissertation, Arizona State University, Tempe.
- Young, J.J., Arrowsmith, J.R., Colini, L., Grant, L.B., 2002. 3-D excavation and measurement of recent rupture history along the Cholame segment of the San Andreas Fault. *Bulletin of the Seismological Society of America* 92, 2670–2688.